Computers and Structures 87 (2009) 758–768

Contents lists available at ScienceDirect

Computers and Structures

journal homepage: www.elsevier.com/locate/compstruc

Numerical study of helicopter blade–vortex mechanism of interaction using large-eddy simulation

Marcel Ilie *

Department of Mechanical and Aerospace Engineering, University of California San Diego, 9500 Gilman Drive #0411, La Jolla, CA 92093, USA

ARTICLE INFO

Article history:
Received 9 June 2008
Accepted 19 November 2008
Available online 25 March 2009

Keywords:
Helicopter blade–vortex interaction
Large-eddy simulation
Smagorinsky model

ABSTRACT

A novel approach, large-eddy simulation, is proposed for the numerical investigation of helicopter blade–vortex mechanism of interaction. The novel approach overcomes all the issues, posed by the other CFD approaches, associated with the vortex dissipation due to the turbulence modeling (RANS, URANS) and computational limitations of DNS. The influence of vertical miss distance and vortex core size on the helicopter blade–vortex mechanism of interaction is subject of investigation. It was observed that the magnitude of the aerodynamic coefficients decreases with the increase of vertical miss distance and the decrease of vortex core size.

1. Introduction

In rotorcraft, blade–vortex interaction is one of the main sources of noise and vibrations and comprises one of the most complex unsteady flow features of helicopter rotor in forward flight. Strong interactions which result in strong chordwise temporal pressure variations are caused by a vortex whose axis is parallel (or nearly parallel) to the spanwise axis of the blade. Seath et al. [1] have shown that the parallel interactions are the most significant when compared with either oblique or perpendicular interactions.

BVI noise occurs mainly during landing/descending flight and sometimes in manoeuvring flight when the rotating blades pass in close proximity to the previously shed rotor tip vortices. These vortices induce sharp periodic aerodynamic disturbances on the blades and generate highly impulsive BVI noise. The radiated noise depends on the blade–vortex vertical miss distance and the characteristics of previously shed vortex. BVI is most prominent during slow-speed descent, since during this phase of the flight the vortex is more likely to interact with the rotor blades. BVI noise is radiated downwards and usually dominates all the other sources of noise, as shown by Papadakis et al. [2]. When a vortex is shed from the rotating blade tip and convected downstream, it is intersected by the next rotor blade. At the start of the BVI, the vortex is at an upstream location and moves towards the airfoil leading edge, as schematically presented in Fig. 1.

For the past two decades, the BVI phenomenon has been investigated both experimentally and numerically. Previous experimental studies have shown that the unsteady lift depends on the vortex characteristics and blade–vortex vertical miss distance. In this sense Abello and George [3,4] have shown that the vortex–airfoil vertical miss distance is a parameter that can be used to control the vortex–airfoil mechanism of interaction. Horner et al. [5] have studied the vortex core distortion during the blade–vortex interaction and showed that the vortex core size is highly distorted for the case of parallel BVI. In spite of the extensive experimental studies of BVI, an accurate prediction of aerodynamic coefficients and aeroacoustic field is still a challenge and subject of debate.

One of the main challenges encountered in the experimental study of BVI is associated with the generation of the upstream vortex. In general the experimental study of BVI involves a two airfoils configuration. The first airfoil is used to generate the upstream vortex, while the second one is subject to BVI. In general the upstream vortex is generated by either pitching or plunging an airfoil. Usually the BVI investigations are performed using the particle image velocimetry (PIV) technique. One of the challenges associated with the generation of the upstream vortex is that the wind tunnel has to be large enough, about 6 m high and 4 m wide, such that there is no wall effect. The wall effect causes a fast dissipation of the vortex before interacting with the second airfoil, Seath et al. [1]. Usually the pitching or plunging airfoil generates large flow disturbances propagating towards the walls. The flow-wall interactions generate large normal velocity components which are responsible for the vortex distortion.

Another challenge is that, a good correlation between the free-stream velocity in the wind tunnel and the strength of the generated vortex must be ensured. It was observed by Horner et al. [5] that if the free-stream velocity is about 50 m/s, the vortex is completely destroyed before the interaction with the second airfoil. It is important to mention here that in general the flow associated

* Tel.: +1 858 534 1466; fax: +1 858 534 7078.
E-mail address: milie@ucsd.edu

0045-7949/$ - see front matter © 2008 Elsevier Ltd. All rights reserved.
doi:10.1016/j.compstruc.2008.11.011

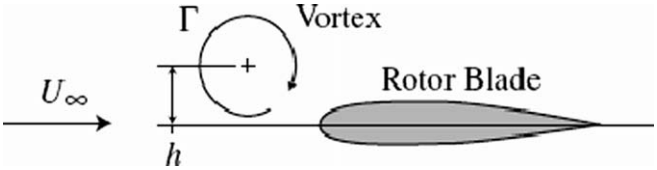

Fig. 1. Schematic view of blade–vortex interaction.

with BVI reaches a velocity of about 100 m/s. This poses a high challenge regarding the generation of the vortex.

Another challenge associated with the experimental investigation of BVI represents the prediction of the aeroacoustic field. Previous experimental studies have shown that it is very difficult to identify the acoustic noise associated with BVI from the one caused by the wind tunnel structural noise, Seath et al. [1], Abello and George [3,4].

Due to all these challenges posed by the experimental study of blade–vortex interaction, the numerical prediction of BVI has emerged as an alternative. Numerical simulation of BVI has been of interest to Computational Fluid Dynamics (CFD) for many years. However, a good understanding and prediction of BVI has not been achieved. Usually, the aerodynamic flows of engineering interest ($Re \sim 10^5 \div 10^6$) are computed using the well-known Reynolds-averaged Navier–Stokes (RANS) approach. The use of RANS approach significantly relies on turbulence models to capture all the relevant turbulence scales. RANS methods predict the noise using the mean flow properties. Due to the fact that noise generation is a multi-scale problem, involving a wide range of length and time scales, the use of RANS-based prediction methods remains limited. Although RANS methods are useful for predicting the aerodynamic coefficients, holding accurately up to some extent, they are usually not suitable or reliable for an accurate noise prediction. On the other hand, Reynolds-averaged Navier–Stokes provides only steady-state solutions of the flow field and aerodynamic coefficients. Since BVI is a time-dependent phenomenon, RANS is not a suitable approach and a time-dependent solution must be sought.

The recent improvements in the processing speed of computers make the applicability of Direct Numerical Simulation (DNS) to turbulent flows more feasible. When using the DNS approach, all the scales of motion are simulated by solving the Navier–Stokes equations. No averaging or approximation is undertaken to solve the governing equations.

Due to the wide range of length and time scales present in turbulent flows, the use of DNS is still limited to low-Reynolds-number flows ($Re \sim 5000$) and relatively simple geometries. It is well-known that the number of grid points required for a DNS solution is proportional to $Re^{9/4}$. Direct Numerical Simulation of high-Reynolds number flows of practical interest would necessitate high resolution grid requirements that are far beyond the capability of the most powerful computers available nowadays.

In order to overcome the grid requirements issues, turbulence has to be modeled in order to perform simulations for problems of practical interest. Accurate prediction of BVI aerodynamic loads and aeroacoustics using unsteady Reynolds-averaged Navier–Stokes (URANS) is known to be very challenging due to the complex unsteady flow dynamics, involving boundary layer development on the suction side and flow separation.

Another challenge posed by the numerical investigation of BVI is the inherent numerical dissipation of CFD turbulence models, which severely affects the preserving of the vortex characteristics. Tung et al. [6] present a comprehensive study of BVI using different CFD approaches and show their highly dissipative nature. In separate studies Felten and Lund [7], Nagarajan and Lele [8] and Lardeau and Leschziner [9] identified the dissipative nature of URANS.

The present research proposes a novel approach for the numerical investigation of blade–vortex interaction based on large-eddy simulation (LES). The motivation for LES is that, since the large energy-carrying eddies are highly influenced by the boundary conditions, they can be computationally resolved while the small eddies or unresolved scales are modeled. In general the large scales of motion are more energetic than the small ones and their size and strength make them the most effective transporters of the conserved properties. Formally large-eddy simulation is a result of space averaging operation applied to Navier–Stokes equations. Roughly speaking, LES is a method that resolves only those turbulent structures (eddies) that can be captured by a certain grid size, while all of the smaller eddies are modeled. The advantage of this method is that it provides much more information than statistical methods (RANS) and it is computationally less expensive than DNS. Large-eddy simulation with a lower computational cost is a promising alternative method to DNS for the numerical investigation of high Reynolds-number flows. LES method is capable of simulating high Reynolds number flows of engineering interest. Since the blade–vortex interaction is an unsteady process, LES is the most affordable computational tool to be used, since it is the only way, other than DNS, to obtain a time-accurate unsteady solution.

The present study of BVI using LES represents a premier to the rotorcraft research community, bringing a significant contribution to the field. The present research overcomes all the issues, posed by the other CFD approaches, associated with the vortex dissipation due to the turbulence modeling (RANS, URANS) and computational limitations of DNS. The present study identifies itself as a significant achievement, mainly by eliminating the issues associated with the vortex dissipation which has been a challenge for decades.

Also, the use of LES in the present research ensures that the boundary layer separation associated with BVI is captured. It is shown in the results section that the flow separation has a significant influence on the aerodynamic coefficients. The capture of boundary layer separation has been a great challenge for the previous studies using URANS, Lardeau and Leschziner [9].

2. Computational method and models

2.1. Computational method

In the present numerical study, the large-eddy simulation (LES) technique is being employed. The motivation for LES is that since the large energy carrying eddies are highly influenced by the boundary conditions they can be computationally resolved while the small eddies or unresolved scales are modeled. In general the large scales of motion are more energetic than the small ones and their size and strength make them the most effective transporters of the conserved properties. Therefore an approach which treats the large eddies more accurately than the small ones would be more suitable. Large-eddy simulation is the approach that would meet this requirement. Large-eddy simulation is a result of space averaging (filtering) operation applied to Navier–Stokes equations. In the present study an implicit filter is used, which means that grid size is acting as filter and consequently all the flow structures smaller than the grid size are modeled. Large-eddy simulation, roughly speaking, is a method that resolves only those turbulent structures (eddies) that can be captured by a certain grid size, while all of the smaller eddies are modeled. The filtered Navier–Stokes equations are:

$$\frac{\partial \bar{u}_i}{\partial x_i} = 0 \tag{1}$$

$$\frac{\partial \bar{u}_i}{\partial t} + \frac{\partial}{\partial x_j}(\bar{u}_i \bar{u}_j) = -\frac{\partial \bar{p}}{\partial x_i} - \frac{\partial \tau_{ij}}{\partial x_j} + \frac{1}{Re}\frac{\partial^2 \bar{u}_i}{\partial x_j \partial x_j} \tag{2}$$

where τ_{ij} is the subgrid scale (SGS) model given by:

$$\tau_{ij} = \bar{u_i u_j} - \bar{u}_i \bar{u}_j \tag{3}$$

and is modeled. In the present study the SGS proposed by Smagorinsky and Lilly [12,13] is used. In the present analysis the value of Smagorinsky constant was set to 0.1. The SGS stresses are related to the strain rate tensor by SGS viscosity, ν_T:

$$\tau_{ij} - \frac{1}{3}\delta_{ij}\tau_{kk} = 2\nu_T \bar{S}_{ij} \tag{4}$$

The SGS viscosity ν_T is given by:

$$\nu_T = \rho(C_s D_{wall}\Delta)^2 |\bar{S}| \tag{5}$$

where C_s is the Smagorinsky constant ($C_s = 0.1$ in the present work), D_{wall} represents the van Driest wall damping factor, Δ is the filter width and $|\bar{S}|$ represents the magnitude of the large-scale strain-rate tensor.

$$\bar{S}_{ij} = \frac{1}{2}\left(\frac{\partial \bar{u}_i}{\partial x_j} + \frac{\partial \bar{u}_j}{\partial x_j}\right) \tag{6}$$

More complex SGS models have appeared in the literature, for example, the dynamic SGS eddy viscosity models [14], but they are beyond the scope of the present work.

2.2. Computational model

In the present analysis, a uniform flow and superimposed vortex past an airfoil NACA0012, is investigated. The computations are carried out for two different BVI studies. The first study concerns the influence of vortex–airfoil vertical miss distance (h) on the vortex–airfoil mechanism of interaction and aerodynamic coefficients. In this sense the computations are performed for three different vertical miss distances $h = 0.00$ m, $h = -0.005$ m and $h = -0.01$ m respectively. In this first study the vortex core size r is equal with 0.2 c where c represents the airfoil chord size and is kept constant throughout the entire study.

The second study concerns the influence of vortex core size on the vortex–airfoil mechanism of interaction. In this sense three different vortex core sizes $r = 0.3$ c, $r = 0.4$ c and respectively $r = 0.5$ c are investigated, where c is the cord of the airfoil.

For all test cases, the release location of the vortex V (x_v, y_v) is (0.13 m, 0.00 m), upstream of the leading edge. No slip boundary conditions are used at the airfoil wall. Free slip boundary conditions are used at the top and bottom walls.

The quasi 3-D simulations were performed for a Reynolds number, $Re = 1.3 \times 10^6$, based on free-stream velocity U_∞ and the chord length of the airfoil. An airfoil with the chord length $c = 0.2$ m is centered in the computational domain whose outer boundary is a square with the sides equal to 9 c and a spanwise size of 3 c. The computational domain consists of 12.6×10^6 grid points, with a cluster of grid points around the airfoil and a grid expansion factor of 0.1. For all the computations in the present analysis, a dimensionless time step $\bar{\Delta t} = \Delta t U_\infty / c = 1 \times 10^{-6}$ is chosen, where U_∞ is the free-stream velocity. The time-step is determined with respect to the explicit time-marching scheme (fourth order Runge-Kutta).

A schematic view of the blade–vortex interaction is presented in Fig. 1. It is important to mention here that although in rotorcraft there is a periodic rotational motion of the blade, for the experimental or numerical investigation of the blade–vortex interaction it can be assumed, without losing any flow physics, that the blade is fixed, as shown by Seath et al. [1], Papadakis et al. [2], Abello and George [3,4], Horner et al. [5], Nagarajan and Lele [8] and Lardeau and Leschziner [9]. The blade can be assumed fixed for the following reason. At the instant of blade–vortex interaction, the most important parameter defining the BVI is the relative velocity between vortex and blade. The relative velocity between vortex and blade is the sum of tangential velocity of the tip of the blade V_{tip} and the actual traveling velocity of the helicopter $V_{helicopter}$, $V_{relative} = V_{tip} + V_{helicopter}$. In the present and previous numerical studies Nagarajan and Lele [8] and Lardeau and Leschziner [9], the blade is assumed fixed. However, the free-stream velocity is imposed such that to equal the vortex-blade relative velocity $V_{relative}$. In this way the vortex travels with the free-stream velocity, encountering the fixed blade.

A blade–vortex interaction study involving a rotating frame would be extremely challenging and out of research for next decades, due to the high computational cost. On the other hand such a study requires large mesh deformations which would result into a loss of solution accuracy since LES requires highly orthogonal grid cells, Wang and Moin [11].

In the present study the numerical simulations were performed as follows. For computational reasons and to achieve a converging solution, faster, the large-eddy simulations were initialized from a converging steady-state solution using Reynolds-averaged Navier–Stokes (RANS). The numerical simulations using the RANS approach were performed for a computational domain consisting of 3.25×10^6 grid points. The computational domain was chosen based on the results indicated by the grid convergence analysis as presented in Fig. 2. The grid convergence analysis suggested large differences of the solutions in the boundary layer region, for grids sizes 5.32×10^5 and 1.389×10^6, and therefore a cluster of grid points was used in this region.

Although a computational domain consisting of 3.2×10^6 seems to be adequate for the present study, a much larger number of grid points 12.6×10^6 was used for the large-eddy simulation investigations. It is well known that generally LES requires very fine meshes [10]. The present grid configuration provides accurate results for the LES study as shown by the grid convergence analysis, Fig. 3. The option for a grid configuration consisting of 12.6×10^6 was motivated by the computational cost. An increase of 80% of the number of grid points would not bring any significant improvement to the solution accuracy; except a much higher computational cost. The difference of the solutions provided by the two grid sizes is very small.

It is important to mention here that in large-eddy simulation the large turbulent scales (the scales larger than the grid size)

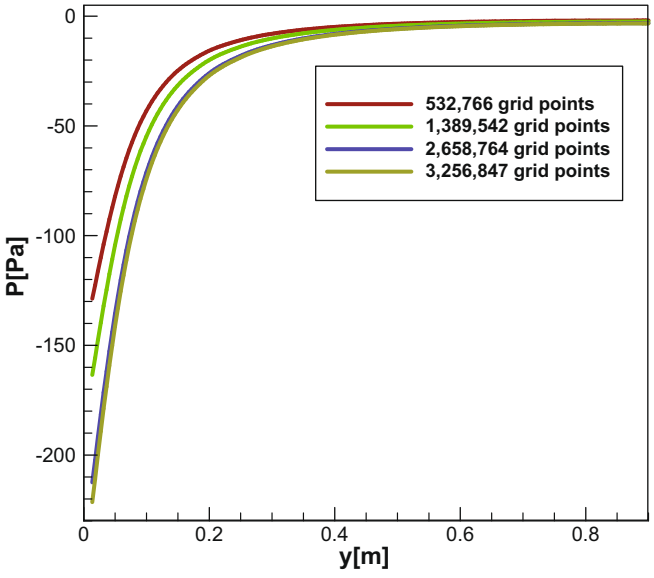

Fig. 2. Grid convergence analysis for RANS simulations.

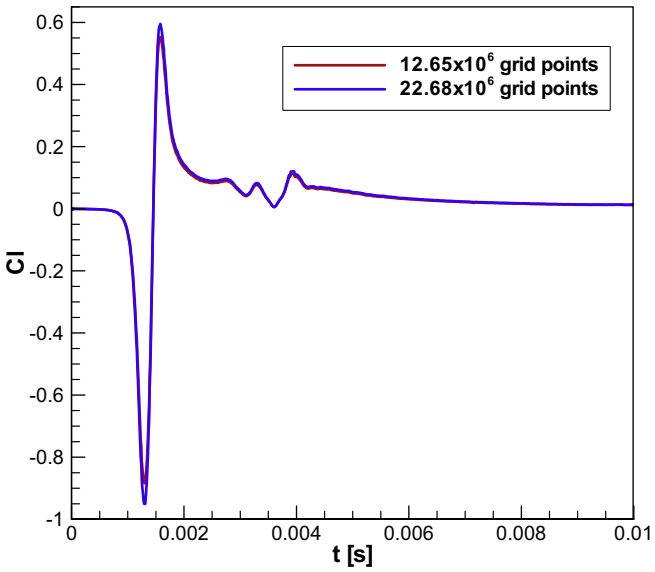

Fig. 3. Grid convergence analysis for LES simulations.

are resolved while the small ones are modeled. Consequently, very fine grids would eliminate the effect of the subgrid scale model and all the turbulent structures are completely resolved. At this stage the solution would be associated with direct numerical simulation (DNS). As already mentioned in the previous section, for high Reynolds number flows, a DNS solution would necessitate high resolution grid requirements that are far beyond the capability of the most powerful computers available nowadays.

3. Results and discussion

The results of the present study are structured as follows. In the first part, the aerodynamic results of a study regarding the influence of vertical miss distance on the vortex–airfoil mechanism of interaction are presented. The second part presents the results regarding the influence of vortex core size on the vortex–airfoil mechanism of interaction.

3.1. Influence of vortex–airfoil vertical miss distance on the mechanism of interaction

In the present study the influence of vertical miss distance on the vortex–airfoil mechanism of interaction is subject of investigation. The vortex core size r is equal with 0.2 c where c represents the airfoil chord size and is kept constant throughout this study. Fig. 4 presents the instantaneous velocity magnitude from a LES solution for three different test cases based on the vortex–airfoil vertical miss distance (h). The velocity magnitude is presented at five different instants in time as a clockwise rotating vortex travels at three different vertical miss distances.

From Fig. 4 it can be seen that as the vortex approaches the airfoil, all test cases present similarities in the sense that the airfoil senses an induced velocity from the vortex pointed downward. Also, the vortex–airfoil mechanism of interaction exhibits a similar behavior at the instant when the vortex encounters the airfoil, $t = 0.0013$ s. From Fig. 4 it is apparent that the vortex core is distorted as the vortex interacts with the airfoil, at instant $t = 0.0013$ s, and there are wake perturbations due to the presence of the residual component of the vortex in the flow field, $t = 0.0044$ s. Also it can be seen that as the vortex approaches the airfoil and travels the chord length of airfoil, the velocity distribution on the upper and lower surface of the airfoil changes continuously until the vortex leaves the airfoil. The upper surface of airfoil experiences a higher velocity associated with flow separation and reverse flow as the vortex travels the chord length of the airfoil. However, increasing the vortex–airfoil vertical miss distance, the lower surface of airfoil senses a higher velocity as the vortex encounters the airfoil. From the time-varying velocity field it can be seen that the offset distance h influences the vortex–airfoil mechanism of interaction in a particular manner.

Due to the vortex–airfoil mechanism of interaction, the vortex splits into two residual components of different strengths and sizes, traveling on two separate paths, one below and the other above the airfoil, as seen at instant $t = 0.0025$ s.

The change in velocity distribution field influences the pressure distribution around the airfoil and causes oscillations of the stagnation point along the upper and lower surface of the airfoil, as seen in Fig. 5. When the vortex is in the length of one chord downstream the airfoil, Fig. 4a, $t = 0.0044$ s, the wake is disturbed by the presence of the residual component of the vortex. As the residual component of the vortex travels far downstream, it merges into the airfoil wake and a significant mixing with the airfoil wake is observed. This mixing causes a fast dissipation of the residual component of the vortex.

From the time history of velocity and pressure fields, for the two test cases $h = 0.00$ m and $h = -0.005$ m, it can be seen that a small change in the vertical miss distance has a significant impact on the vortex–airfoil mechanism of interaction. From Fig. 4b, it can be seen that for a vertical miss distance $h = -0.005$ m, the lower surface of airfoil senses a higher induced velocity as the vortex travels the chord length of the airfoil. Due to the vortex–airfoil mechanism of interaction, the vortex splits into two residual components of different strengths, traveling on two different paths, one below and the other above the airfoil wake. The residual component of vortex that travels below the airfoil wake has a higher strength and this is a result of the vortex–airfoil mechanism of interaction. As the two residual components of the vortex travel downstream the airfoil, they merge into the airfoil wake. The merging process between the residual components of the vortex and airfoil wake is associated with strong mixing which is responsible for the fast dissipation of the residual component of the vortex.

For a vertical miss distance $h = -0.01$ m, due to the vortex–airfoil mechanism of interaction, two counter-rotating vortices of different strengths are formed. This is observed in both, velocity and pressure fields, Figs. 4c and 5c, at the instant $t = 0.0035$ s. The two newly generated vortices travel on a path under the airfoil wake. Also for test case $h = -0.01$ m, the two newly generated vortices have a higher strength than the ones observed for test case $h = -0.005$ m and this is due to the vortex–airfoil mechanism of interaction, defined by the vortex–airfoil vertical miss distance. As the two newly generated counter-rotating vortices travel far downstream the airfoil, they interact with the airfoil wake and distort it.

The present study shows that the vortex–airfoil mechanism of interaction influences both velocity and pressure fields and implicitly influences the aerodynamic coefficients as well. From Figs. 4b and 4c, it can be seen that when the vortex is in the neighborhood of airfoil, passing underneath of airfoil ($t = 0.0025$ s), due to the mechanism of interaction, the vortex is highly distorted and as a result disturbs the near region flow field.

Similarly to velocity field, the vortex–airfoil mechanism of interaction influences the pressure field as well. From Fig. 5 it can be seen that there is a large pressure unbalance at the upper and lower surface of airfoil, at the instant when the vortex encounters the airfoil, and a region of low pressure is observed under the lower surface of the airfoil. This is associated with a decrease of lift coefficient as the vortex encounters the airfoil. It can be seen that

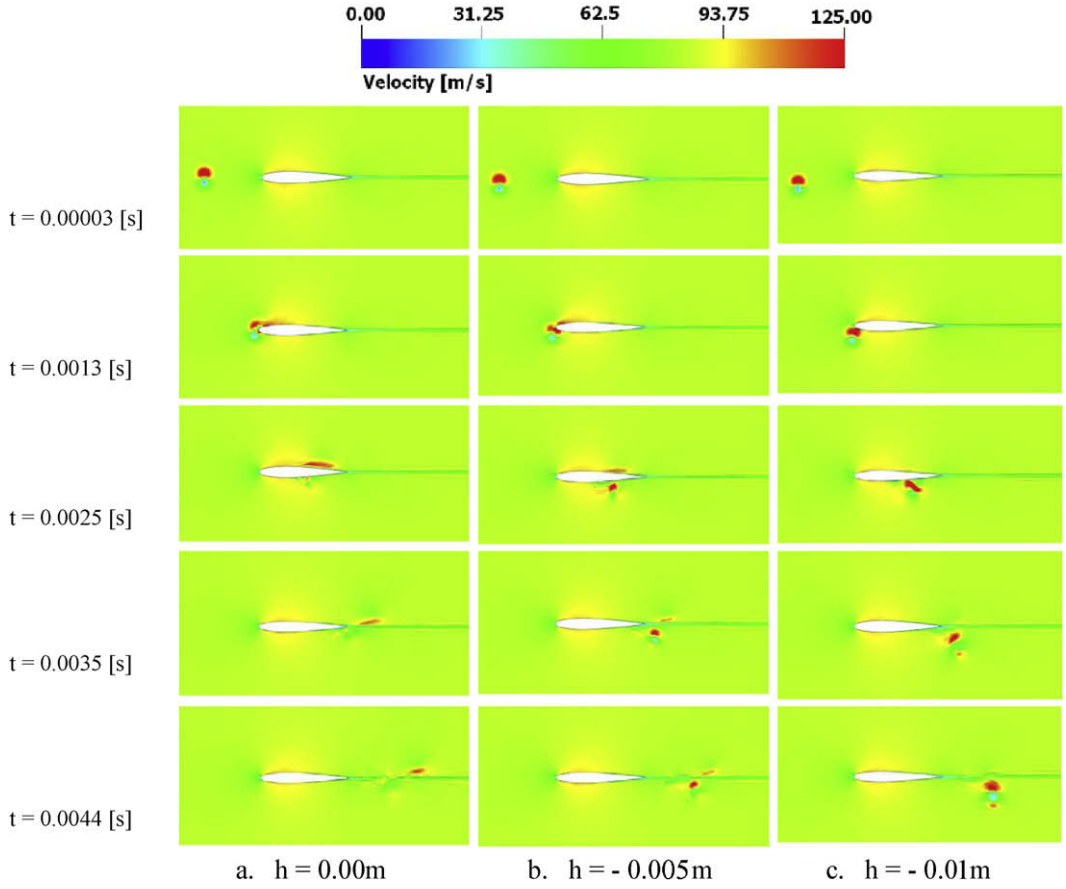

Fig. 4. Time-evolved fluid structures (velocity magnitude).

this low pressure region is larger for the case of a vertical miss distance $h = 0.00$ m and decreases as the vertical miss distance increases, as seen in Fig. 5 at the instant $t = 0.0013$ s. As the residual component of the vortex travels the chord length of airfoil, the flow field recovers and the balance of pressure at the upper and lower surface of airfoil is restored, as seen in Fig. 5 at instant $t = 0.0035$ s.

For a vortex–airfoil vertical miss distance $h = 0.00$ m, the interaction is the most significant and the vortex is severely distorted. The vertical miss distance defines the vortex–airfoil mechanism of interaction. In this sense, from the pressure field, two distinctive vortices of different strengths are identified for a vertical miss distance $h = -0.01$ m at the instant $t = 0.0035$ s. From Fig. 5 it can be seen that as the vortex encounters the airfoil there is a continuous change of pressure distribution at the airfoil surface.

The time-varying pressure causes the stagnation point to move from the upper surface to the leading edge and then toward the lower surface. This movement of the stagnation point affects the lift on the blade. The rate of change of lift is related to the pressure propagated to an observer. The unsteady vortex motion induces pressure fluctuations in the proximity of the blade and results in a series of expansion/compression waves. The change in pressure at the instant when the vortex encounters the airfoil is associated with the BVI noise.

The time-varying pressure field influences the aerodynamic coefficients in a particular manner and this is detailed in the following. Fig. 6 presents the temporal variation of lift coefficient for the case of a vortex superimposed on a uniform flow encountering a NACA 0012 airfoil at a zero angle of attack and a vertical miss distance $h = 0.00$ m. The lift coefficient is influenced by the pressure distribution over the airfoil surface. From Fig. 6, it can be seen that there is a continuous decrease of lift coefficient as the vortex approaches the airfoil (until a minimum value is achieved), followed by a sudden jump as the vortex core passes the airfoil leading edge. This sudden jump in lift coefficient is associated with a sudden change in the pressure field. The sudden change in pressure has an aeroacoustic meaning and it is associated with the blade–vortex interaction (BVI) aeroacoustic noise, at the instant when the vortex encounters the airfoil. Although an increase of lift coefficient value is observed as the vortex passes the leading edge, the absolute value of this maximum is smaller than the absolute minimum value previously described. This difference between minimum and maximum absolute values is associated with the vortex core distortion when the vortex encounters the airfoil. When the residual component of the distorted vortex is far downstream from the airfoil, the lift coefficient converges asymptotically to a zero value and the flow field is almost undisturbed. It is worth to notice that for a value of vortex–airfoil vertical miss distance $h = 0.00$ m, although the amplitudes of lift coefficient are high, the fluctuations of lift coefficient when the vortex travels the chord length of airfoil are small and this is a result of the vortex core distortion as well. Also for a vertical miss distance $h = 0.00$ m, fluctuations of lift coefficient are observed at the instant when the residual component of the distorted vortex leaves the airfoil and merges into the airfoil wake, at the instant $t = 0.0035$ s.

Similar behavior of the lift coefficient was observed for the other two test cases $h = -0.005$ m and $h = -0.01$ m. However, there are some differences associated with the vortex–airfoil mechanism of interaction and these are better assessed by the comparison of lift coefficient values. In this sense, Fig. 7 presents a comparison

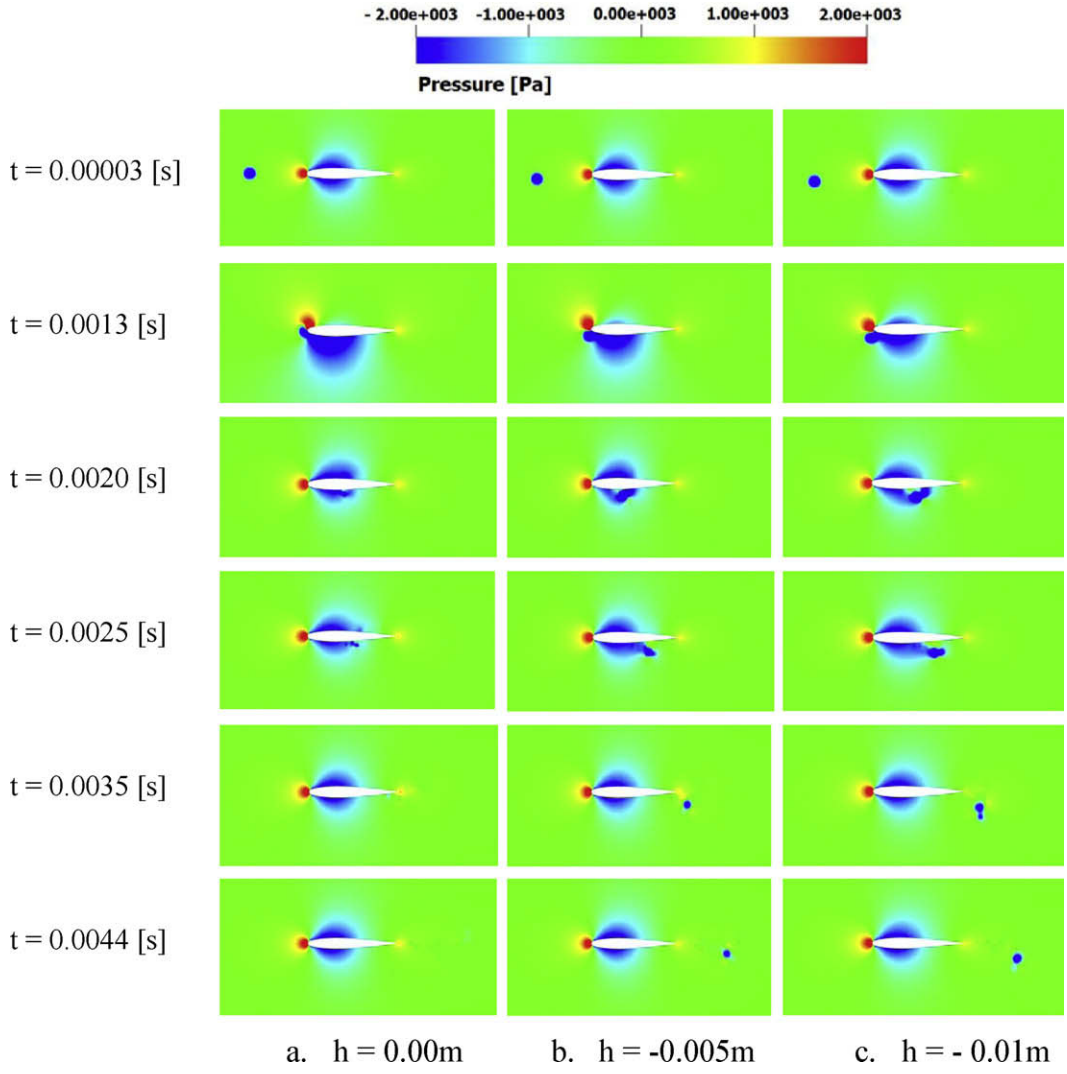

Fig. 5. Time-evolved fluid structures (pressure field).

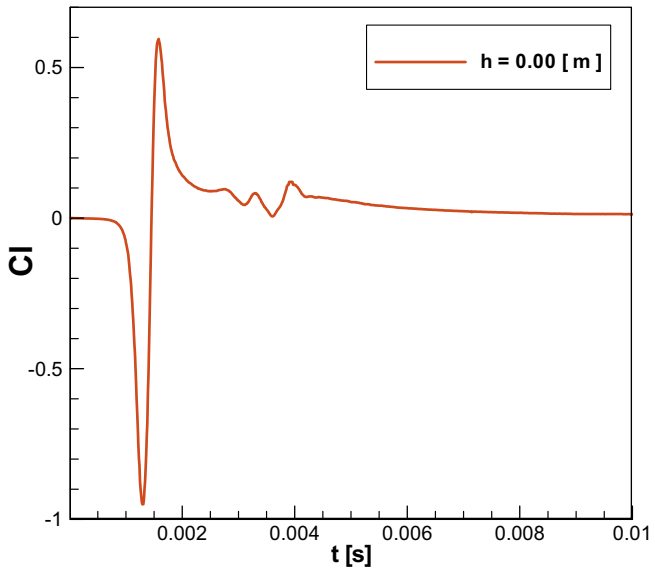

Fig. 6. Time history of lift coefficient.

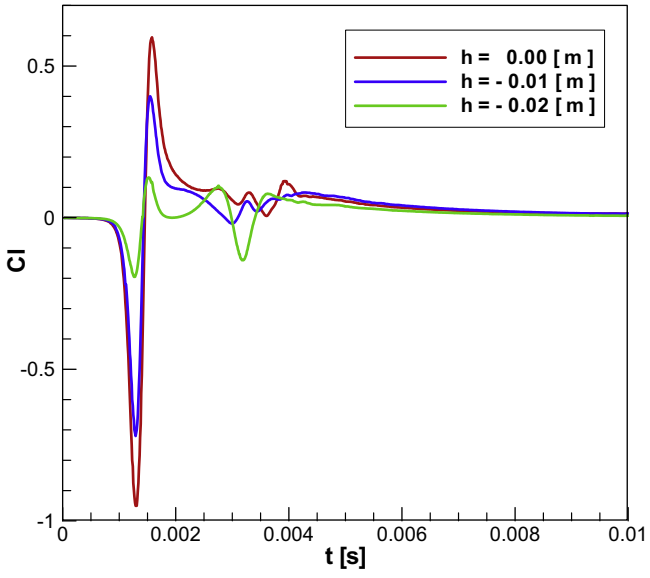

Fig. 7. Comparison of time-varying lift coefficient.

of the lift coefficient for three different vortex–airfoil vertical miss distances $h = 0.00$ m, $h = -0.005$ m and $h = -0.01$ m.

For all test cases, the lift coefficient presents a sudden jump at the instant when the vortex encounters the airfoil ($t = 0.0013$ s). The amplitude of the jump in lift coefficient decreases as the vortex–airfoil vertical miss distance increases. This decrease is due to the fact that the vortex–airfoil interactions are less significant and have less impact on the flow field. From the comparison of lift coefficient, it can be seen that with the increase of vortex–airfoil vertical miss distance, the jump in lift coefficient at $t = 0.0013$ s tends to become more symmetric with respect to a zero value and the transition from negative to positive values is smoother.

Large fluctuations in lift coefficient are observed at the instant when the vortex travels the airfoil chord length for a vertical miss-distance $h = -0.01$ m. This is a consequence of the fact that the vortex–airfoil interactions are less and less severe; the vortex preserves better its characteristics (strength and core size) and has a more significant influence on the flow field. As the vortex travels downstream the airfoil, the lift coefficient decays asymptotically to zero from positive values, for all test cases.

Similar to the lift coefficient, the presence of the vortex in the flow field influences the drag coefficient as well. For the case of a uniform flow past a NACA 0012 airfoil, at angle of attack $\alpha = 0°$, the drag coefficient is constant and has the value of $C_d = 0.006$ for a Reynolds number 1.3×10^6.

Fig. 8 presents the time-varying drag coefficient for the case of a vortex superimposed on uniform flow encountering a NACA 0012 airfoil at a zero angle of attack and a vertical miss distance $h = 0.00$ m. At the instant when the vortex encounters the airfoil ($t = 0.0013$ s) separation occurs. As a result of the vortex–airfoil mechanism of interaction, reverse flow is observed, and this is indicated by the negative values of drag coefficient. The vortex–airfoil mechanism of interaction has a significant impact on the drag coefficient, reflected by the large negative value of drag coefficient $C_d = -0.163$. Oscillations of drag coefficient are observed as the vortex travels the first half of the airfoil chord length, at the instant $t = 0.0016$ s. As the residual component of the vortex travels downstream the airfoil, the drag coefficient reaches a constant value of $C_d = 0.006$, which corresponds to the case of uniform flow past a NACA 0012 airfoil, at angle of attack $\alpha = 0°$.

Fig. 9 presents the comparison of time-varying drag coefficient for three different test cases, based on the vortex–airfoil vertical

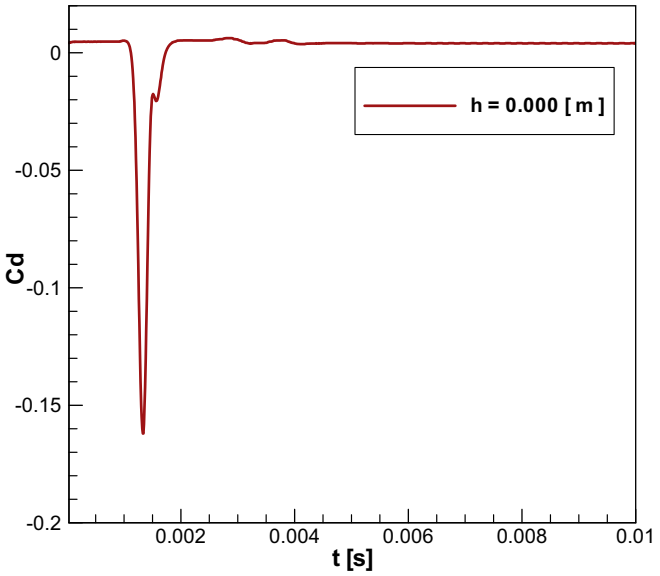

Fig. 8. Time history of drag coefficient.

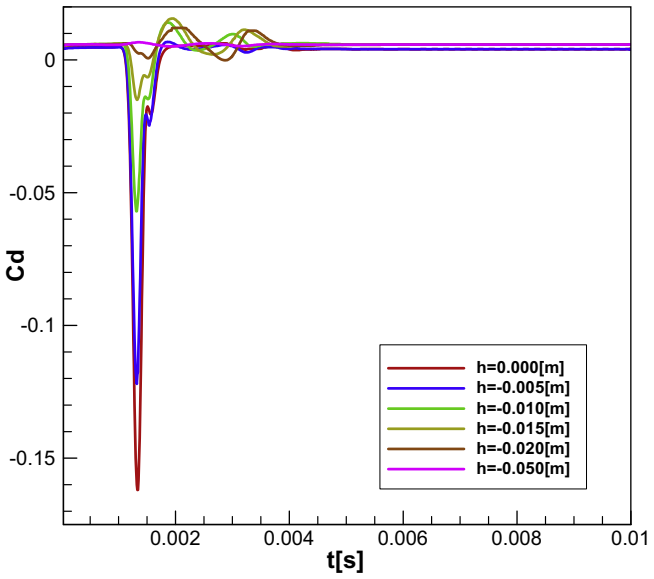

Fig. 9. Comparison of time-varying drag coefficient.

miss distance h. For most of test cases, large negative values of drag coefficient are observed at the instant when the vortex encounters the airfoil, $t = 0.0013$ s. These negative values are primarily caused by the flow separation and reverse flow at the surface of airfoil. It can be seen that the largest amount of reverse flow occurs when the vortex–airfoil vertical miss distance h is small. For the case of vertical miss distance, $h = 0.00$ m, the vortex encounters the airfoil frontally and the interaction is very strong causing a severe distortion of the vortex.

As the vortex–airfoil vertical miss distance increases, the interactions are less and less severe and likewise the separation, resulting in a decay of magnitude of these negative peaks of drag coefficient associated with reverse flow.

From Fig. 9 it can be seen that a small change in the vortex–airfoil vertical miss distance has a large impact on the drag coefficient at the instant when the vortex encounters the airfoil, $t = 0.0013$ s. Due to the vortex–airfoil mechanism of interaction, the distorted vortex causes fluctuations of drag coefficient as it travels the chord length of airfoil. From the drag coefficient comparison, Fig. 9, an increase of the fluctuations of drag coefficient with the increase of vortex–airfoil vertical miss distance is observed, as the vortex travels the chord length of the airfoil. This is a consequence of the influence of vortex–airfoil vertical miss distance, h, on the mechanism of interaction.

Increasing the vortex–airfoil vertical miss distance, the interaction becomes less and less severe; the vortex preserves better its characteristics and has a more significant impact on the flow field. As the residual component of the vortex leaves the airfoil, the drag coefficient reaches a constant value $C_d = 0.006$ which corresponds to the case of a uniform flow past a NACA 0012 airfoil, at angle of attack $\alpha = 0°$, for a Reynolds number 1.3×10^6.

3.2. Influence of vortex core size on the vortex–airfoil mechanism of interaction

Previous studies have indicated that the core size of the vortex, shed from the tip of the blade, grows exponentially in time [14]. Therefore it is of aerodynamic interest to investigate the influence of vortex core size on the vortex–airfoil mechanism of interaction. In the following, a study regarding the influence of vortex core size on the vortex–airfoil mechanism of interaction is conducted.

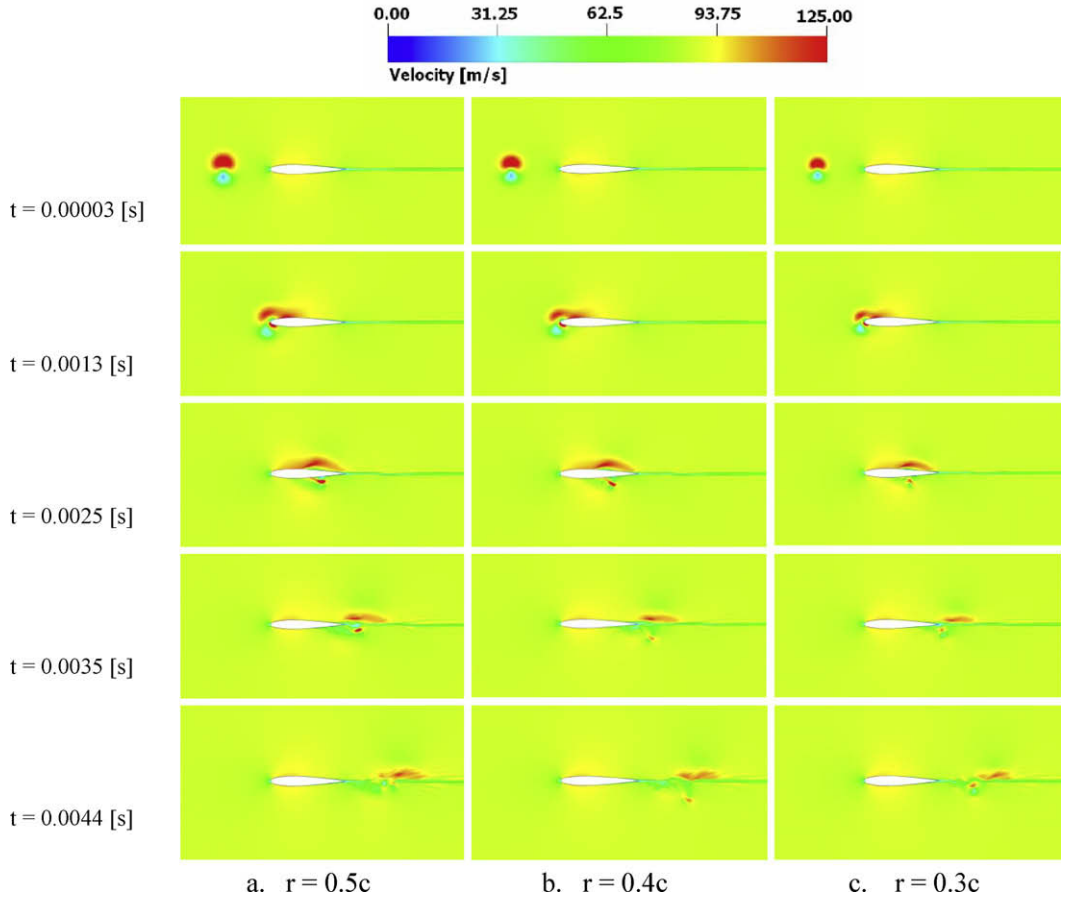

Fig. 10. Time-evolved fluid structures (velocity magnitude).

Fig. 10 presents the instantaneous velocity magnitude from a LES solution, for an angle of attack $\alpha = 0°$, at five different instants in time, as a clockwise rotating vortex travels at the vertical miss distance, $h = 0.00$ m.

Overall the velocity field is very similar with the one described in Section 3.1. From Fig. 10 it can be seen that independent of the vortex core size, the vortex is distorted as interacts with the airfoil and there are wake perturbations due to the residual component of the vortex. However, the influence of vortex core size is reflected into vortex–airfoil mechanism of interaction and implicitly into the trend and magnitude of the aerodynamic coefficients. From the time-varying velocity field it can be seen that the vortex core size influences the vortex–airfoil mechanism of interaction in a particular manner.

Due to the vortex–airfoil mechanism of interaction, the vortex splits into two residual components of different strengths and sizes, which travel on two separate paths, one below and the other above the airfoil, as seen at instant $t = 0.0025$ s.

For all test cases, the residual component of the vortex that travels underneath of the airfoil has a lower magnitude than the one traveling above the airfoil. From the velocity field it can be seen that the strength and size of the vortex residual components decrease with the decrease of vortex core size. For all test cases, at the instants $t = 0.0025$ s and $t = 0.0035$ s, two residual components of the distorted vortex are observed, Fig. 10. It is worth to notice that for a vortex core size $r = 0.5$ c, the residual component of the vortex that travels underneath of the airfoil, merges into the airfoil wake and dissipates, as seen in Fig. 10a, at instant $t = 0.0044$ s. Also from Fig. 10 it can be seen that for a vortex core size $r = 0.4$ c, the residual component of the vortex which travels underneath of the airfoil distances from the airfoil wake, while for a vortex core size $r = 0.3$ c, the correspondent residual component of the vortex travels on a path close to the airfoil wake. When the residual component of vortex is in the length of one chord downstream the airfoil, it disturbs the airfoil wake as seen in Fig. 10 at the instant $t = 0.0044$ s. As the residual component of the vortex travels farther downstream, it merges into the airfoil wake and a significant mixing with the airfoil wake is observed, causing a fast dissipation of the residual component of the vortex.

The change in velocity field distribution influences the pressure distribution around the airfoil and causes fluctuations of the stagnation point along the upper and lower surface of the airfoil, as seen in Fig. 11. This movement of the stagnation point affects the lift on the blade. The rate of change of lift is related to the pressure propagated to an observer. The unsteady vortex motion induces pressure fluctuations in the proximity of the blade and results into a series of expansion/compression waves which propagate upstream.

The vortex–airfoil mechanism of interaction has impact on both velocity and pressure field and implicitly influences the aerodynamic coefficients as well and this is illustrated in Figs. 12 and 13.

Fig. 12 presents the temporal variation of lift coefficient for the case of a superimposed vortex having a core size $r = 0.5$ which interacts with a NACA 0012 airfoil at a zero angle of attack. The lift coefficient is influenced by the pressure distribution over the airfoil surface. From Fig. 12, it can be seen that there is a continuous decay of lift coefficient as the vortex approaches the airfoil, followed by a sudden jump as the vortex core passes the airfoil leading edge. When the residual component of the distorted vortex is

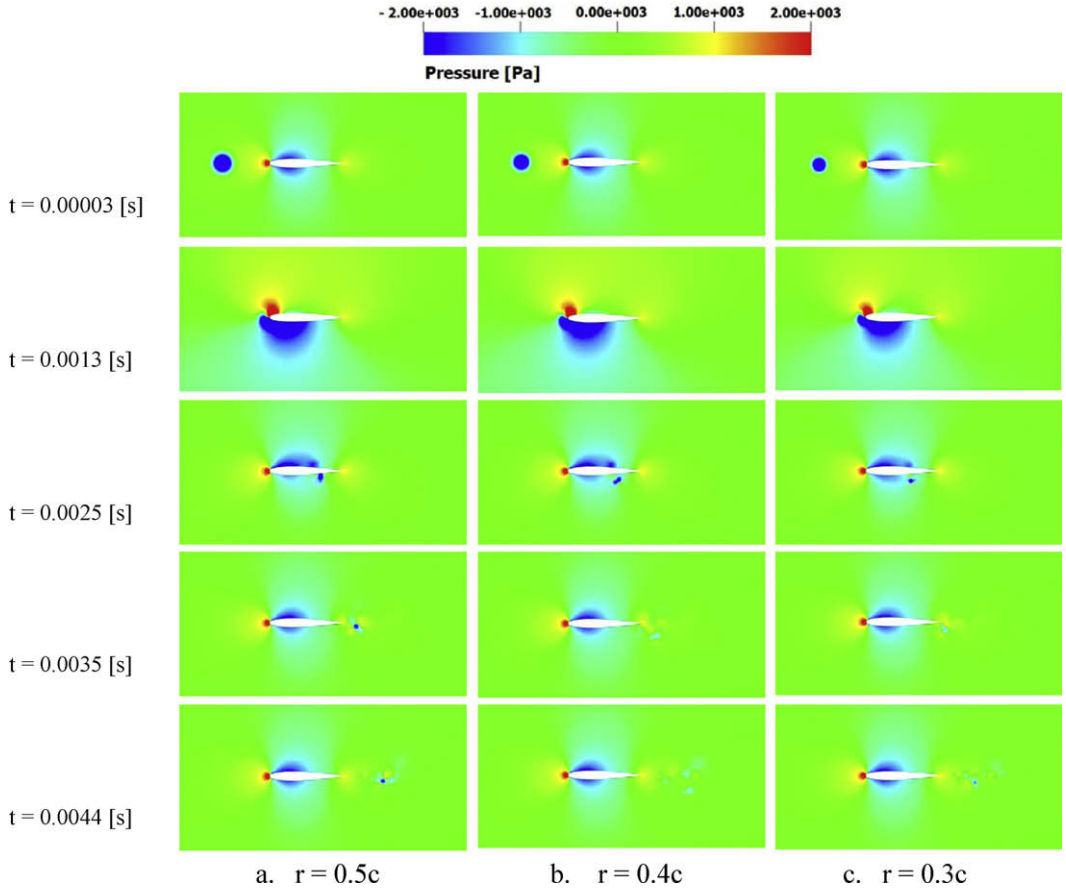

Fig. 11. Time-evolved fluid structures (pressure field).

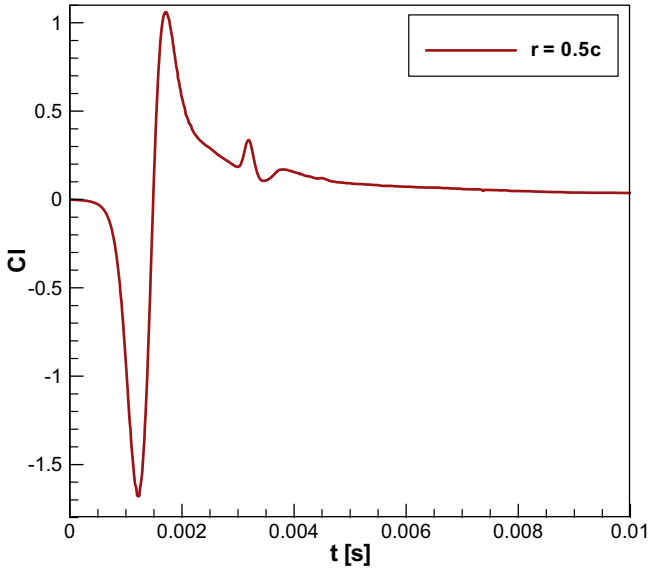

Fig. 12. Time history of lift coefficient.

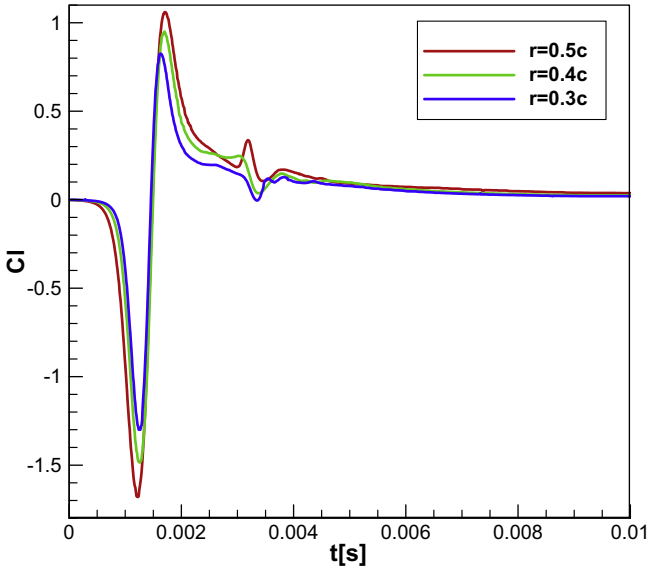

Fig. 13. Comparison of time-varying lift coefficient.

far downstream from the airfoil, the lift coefficient converges asymptotically to a zero value and the flow field near the airfoil surface is almost undisturbed.

Similar behavior of lift coefficient was observed for the other two test cases $r = 0.4$ c and $r = 0.3$ c, and a comparison is presented in Fig. 13.

For all test cases, the lift coefficient presents a sudden jump at the instant when the vortex encounters the airfoil ($t = 0.0013$ s). The amplitude of the jump in lift coefficient decays with the decrease of vortex core size. This decay is due to the fact that the vortex–airfoil interactions are less severe and have less impact on the flow field. It is worth to notice that for all test cases there are

fluctuations in lift coefficient as the residual component of the vortex leaves the airfoil and merges into the airfoil wake, $t = 0.0032$ s. Also, the fluctuations of lift coefficient, at the instant when the residual component of the vortex leaves the airfoil, decay with the decrease of vortex core size. As the residual component of the vortex travels away from the airfoil, the lift coefficient converges asymptotically to zero, from positive values, for all test cases.

Similar to the lift coefficient, the presence of the vortex in the flow field influences the drag coefficient as well. For the case of uniform flow past a NACA 0012 airfoil, at angle of attack $\alpha = 0°$, the drag coefficient is constant and has the value of $C_d = 0.006$, for a Reynolds number 1.3×10^6. The temporal variation of drag coefficient for test case 1 ($r = 0.5$ c) is presented in Fig. 14.

At the instant when the vortex interacts with the airfoil, separation is observed, Fig. 14. As a result of the vortex–airfoil mechanism of interaction reverse flow is observed and this is indicated by the negative values of drag coefficient. The vortex–airfoil mechanism of interaction has a significant impact on the drag coefficient, reflected by the large negative value of drag coefficient, $C_d = -0.67$. Oscillations of drag coefficient are observed as the vortex travels the first half of the chord length of the airfoil, at the instant $t = 0.0016$ s. As the residual component of the vortex travels downstream the airfoil, the drag coefficient reaches a constant value of $C_d = 0.006$.

Fig. 15 presents the comparison of time-varying drag coefficient for three different test cases, based on the vortex core size, $r = 0.5$ c, $r = 0.4$ c and respectively $r = 0.3$ c. For all test cases, large negative values of drag coefficient are observed at the instant when the vortex encounters the airfoil, $t = 0.0013$ s. These negative values are caused by flow separation and reverse flow over the surface of the airfoil. The amount of reverse flow is proportional with the vortex core size. Hence, the largest amount of reverse flow is observed for a vortex core size $r = 0.5$ c. As the vortex core size decreases, the vortex–airfoil interactions are less and less severe and likewise the separation, resulting in a decay of magnitude of these negative peaks of drag coefficient associated with reverse flow. A small change in the vortex core size has a large impact on the drag coefficient at the instant when the vortex encounters the airfoil. Due to the vortex–airfoil mechanism of interaction, the distorted vortex causes fluctuations of drag coefficient as it travels the chord length of airfoil. As the residual component of the vortex leaves the airfoil,

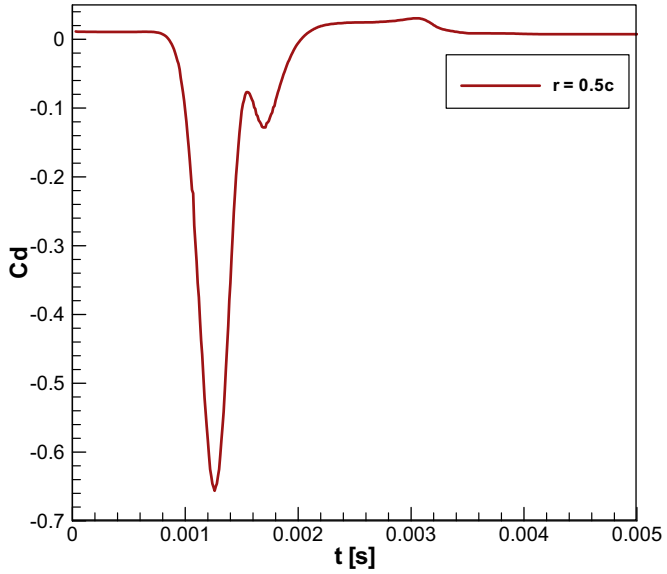

Fig. 14. Time history of drag coefficient.

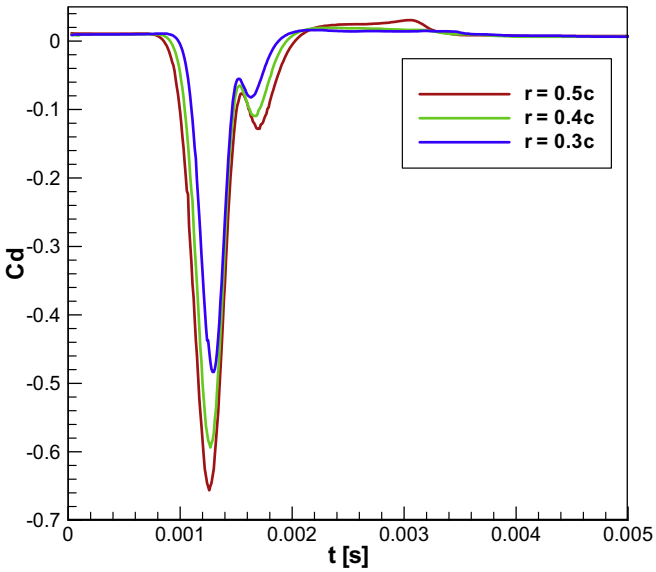

Fig. 15. Comparison of time-varying drag coefficient.

the drag coefficient reaches a constant value $C_d = 0.006$ which corresponds to the case of a uniform flow past a NACA 0012 airfoil at angle of attack $\alpha = 0°$, for a Reynolds number 1.3×10^6. From the drag coefficient comparison, Fig. 15, it can be seen that for the case of a vortex core size $r = 0.5$ c, the drag coefficient presents a slightly higher value at the instant when the vortex leaves the airfoil and this is due to the vortex core size and implicitly to the vortex–airfoil mechanism of interaction.

4. Conclusions

The present research proposes a novel technique, large-eddy simulation (LES), for the numerical investigation of rotorcraft blade–vortex interaction. LES is a method that resolves only those turbulent structures (eddies) that can be captured by a certain grid size, while all of the smaller eddies are modeled. The advantage of this method is that it provides much more information than statistical methods (RANS) and it is computationally less expensive than direct numerical simulation (DNS).

The present research overcomes all the issues posed by the other CFD approaches associated with the vortex dissipation due to the turbulence modeling (RANS, URANS) and computational limitations of DNS. Numerical studies of blade–vortex interaction were conducted to investigate the influence of the vortex–airfoil vertical miss distance and vortex core size on the vortex–airfoil mechanism of interaction and aerodynamic coefficients, for a Reynolds number $Re = 1.3 \times 10^6$. The numerical studies were based on the large-eddy simulation approach.

Investigations were carried out for six different BVI problems, based on the vortex–airfoil vertical miss distance and vortex core size. The presence of the vortex in the flow field induces a velocity at the surface of airfoil and generates time-varying aerodynamic coefficients. The vortex–airfoil mechanism of interaction causes flow separation and reverse flow.

The variation of the aerodynamic coefficients depends on the vortex–airfoil mechanism of interaction defined by the both parameters, vortex–airfoil vertical miss distance and vortex core size. A decrease in magnitude of aerodynamic coefficients with the increase of vertical miss distance was observed. A decrease in the magnitude of aerodynamic coefficients with the decrease of vortex core size was observed as well.

References

[1] Seath D, Kim J, Wilson D. Investigation of parallel blade–vortex interaction at low speed. J Aircraft 1989;4:328–33.
[2] Papadakis M, Nizampatnam L, Hoffmann K. Computational investigation of blade vortex interaction noise. In: Proceedings of the 38th aerospace sciences meeting and exhibit, Reno (NV). AIAA paper 99-0231; January 10–13 2000.
[3] Abelló JC, George AR. Rotorcraft BVI noise reduction by attitude modification. In: Paper presented at the 5th AIAA/CEAS aeroacoustics conference, Bellevue, Washington; May 10–12 1999.
[4] Abello J, George A, Wake displacement study of attitude and flight parameter modifications to reduce rotorcraft blade–vortex interaction (BVI) noise. In: Ninth AIAA/CEAS aeroacoustics conference, Hilton Head, SC; May12–14 2003.
[5] Horner M, Galbraith R, Coton F. Examination of vortex deformation during blade–vortex interaction. AIAA J 1996;6:1188–94.
[6] Tung C, Yu Y, Low S. Aerodynamic aspects of blade–vortex interaction (BVI). In: AIAA, 27th fluid dynamics conference, New Orleans, LA; June 17–20 1996.
[7] Felten F, Lund T. Numerical simulation of parallel airfoil/vortex interaction using a zonal hybrid RANS/LES method. AIAA 2005:5127.
[8] Nagarajan S, Lele S. Prediction of sound generated by a pitching airfoil: a comparison of RANS and LES. In: Twelfth AIAA/CEAS aeroacoustics conference, Cambridge, MA; May 8–10 2006.
[9] Lardeau S, Leschziner MA. Unsteady Reynolds-averaged Navier–Stokes computations of transitional wake/blade interaction. AIAA 2004;42:1559–71.
[10] Strawn RC, Ahmad J, Duque EPN. Rotorcraft aeroacoustics computations with overset grid CFD methods. In: Proceedings of the 54th AHS annual forum, Washington, DC; May 22–24 1996.
[11] Wang M, Moin P. Computation of trailing-edge flow and noise using large-eddy simulation. AIAA J 2000;12:324–39.
[12] Smagorrinsky JS. General circulation experiments with the primitive equation. Monthly Weather Rev 1963;91:99–164.
[13] Lilly DK. On the application on the eddy viscosity concept in the inertial sub-range of turbulence. NCAR manuscript; 1996. p. 195–200.
[14] Germano M, Piomelli U, Moin P, Cabot WH. A dynamic subgrid-scale eddy viscosity model. Phys Fluids A 1991;3(7):1760–5.